AIP | Journal of Applied Physics

Mapping of femtosecond laser-induced collateral damage by electron backscatter diffraction

Anish Kumar and Tresa M. Pollock

Citation: J. Appl. Phys. **110**, 083114 (2011); doi: 10.1063/1.3653839
View online: http://dx.doi.org/10.1063/1.3653839
View Table of Contents: http://jap.aip.org/resource/1/JAPIAU/v110/i8
Published by the AIP Publishing LLC.

Mapping of femtosecond laser-induced collateral damage by electron backscatter diffraction

Anish Kumar[1,2,a] and Tresa M. Pollock[1,3]
[1]*Department of Materials Science and Engineering, University of Michigan, Ann Arbor, Michigan 48109, USA*
[2]*Metallurgy and Materials Group, Indira Gandhi Centre for Atomic Research, Kalpakkam 603102, Tamil Nadu, India*
[3]*University of California, Santa Barbara, California 93106, USA*

(Received 2 June 2011; accepted 15 September 2011; published online 25 October 2011)

The distribution of the collateral damage beneath craters produced by ultrafast (femtosecond) laser single pulses in a nickel base superalloy single crystal has been analyzed using electron backscatter diffraction. The procedure is based on measurements of the localized crystal rotations caused by the dislocations generated by the shock wave that is produced as an effect of laser pulse interaction with a material. Damage in the form of lattice misorientation created by excess dislocations was negligible at laser fluences up to 2 J/cm^2. At higher fluences (5.1-41 J/cm^2), the depth of the damage zone beneath the crater increased linearly with laser fluence. Based on lattice misorientation, excess dislocation densities as high as 3×10^{10}/cm^2 are calculated to be present below the ablated surface in the high fluence regime. © *2011 American Institute of Physics*. [doi:10.1063/1.3653839]

I. INTRODUCTION

The rapid advances in the generation and amplification of ultrashort laser pulses have opened up many new possibilities in laser–matter interaction and materials processing.[1,2] The energy deposition that occurs by application of ultrashort laser pulses is highly spatially concentrated into the material over a short time span and ablation occurs without interaction of the incoming pulse with the ablated material. As a result, only very limited damage in the form of heat-affected zones (HAZ), melting or dislocations occurs over a wide range of fluence.[2,3] The primary mechanism for energy deposition into the bulk of the material is the shock wave rather than thermal transport that is dominant in longer laser pulses.[4]

Although extensive recent studies using scanning electron microscopy (SEM) and atomic force microscopy (AFM) on the ablated surfaces have revealed various aspects of the surface morphology following the ablation process,[2,5–9] only limited work has been conducted to study the subsurface collateral substructural damage following material removal.[3,9,10] Femtosecond laser ablation studies on transmission electron microscopy (TEM) thin foils revealed a very limited (<5 μm) laser-induced plastically deformed layer in superalloys[9] and aluminum.[3] In a few other studies,[10,11] the evolution of the dislocation structure within a laser damaged region has been studied by TEM. However, complete characterization of the distribution of the substructural collateral damage in terms of the dislocation content beneath a crater produced by a laser pulse has not been reported so far for any material.

TEM and electron backscatter diffraction (EBSD) are the two techniques with sufficient sensitivity at the smallest length scales for mapping plastic deformation caused by a laser pulse. Even though TEM can provide direct observation of the local dislocation structure, the volume of material that can be examined is limited, and it is therefore not possible to map the strain distribution over the $\sim\mu$m^3 of material affected by the laser pulse. Hence, EBSD has been used in the present investigation to map the collateral damage caused by single fs laser pulses of varying intensities. The EBSD approach has been used extensively in the past two decades for studying the extent of plastic deformation within individual grains and near the grain boundaries in polycrystals.[12–14] Recently, EBSD has also been used for mapping deformation induced rotation patterns below nanoindents[15] and microindents.[16] The pattern quality and the local crystal rotation are the two parameters derived from the EBSD analysis that can be used to map plastic deformation.[17] As the localized crystal rotation can potentially be linked quantitatively to the local excess dislocation density,[12,17] it has been used in the present investigation for mapping the damage caused by fs single laser pulse of various fluence values.

II. EXPERIMENTAL

The material investigated in this study is a second-generation single-crystal nickel-base alloy, designated CMSX-4. The nominal composition (wt. %) of the alloy is 61.42% Ni, 9.6% Co, 6.6% Ta, 6.4% Cr, 6.4% W, 5.64% Al, 2.9% Re, 1.03% Ti, and 0.1% Hf. Further details of sample heat treatment and microscructure are provided elsewhere.[5] A sample of dimensions $15 \times 6 \times 4$ mm with [001] crystal direction oriented normal to the sample surface was sliced from a single crystal bar for laser machining. The sample was prepared by conventional metallographic procedures with a final polish of 0.25 μm diamond suspension. The fs laser single pulse ablation study was conducted in air using a commercially available Ti:Sapphire laser system, Clark-MXR CPA-2001 (Clark-MXR, Inc., Dexter, MI). The laser

[a]Electronic mail: anish@igcar.gov.in.

pulses were linearly polarized at a wavelength of 780 nm, pulse duration of 150 fs, and were delivered to the sample at a repetition rate of 125 Hz at various average power intensities in a range of 1.5-68 mW. One hundred shots of single pulses at each average power were deposited in a 10×10 array (Fig. 1) at a spacing of 0.1 mm or 0.2 mm, with larger spacing for higher power shots. The sample was ultrasonically cleaned in methanol to remove most of the debris and the ablation features were studied using SEM. The diameter of a circle of the same area as that of the ablated area is taken as the equivalent diameter of the laser ablated area. After the SEM characterization of the ablation features, a thin surface layer of nickel was deposited by electroless plating using Elnic solution (supplied by MacDermid Industrial Solution) to protect the ablation features at and near the edge of the sample while polishing the cross-section for EBSD characterization (Fig. 1). After the nickel plating, the cross-section of the sample was prepared by conventional metallographic procedures with a final polish of 0.25 μm diamond suspension followed by vibratory polishing in 0.05 μm colloidal silica solution for about 4-6 h. EBSD data were acquired using a Philips XL30 FEG SEM with a sample tilt of 70° at 18 mm working distance. The SEM was operated at 20 kV and the data were acquired at 0.06-0.18 μm step size. The grain reference orientation deviation (GROD) function available in the EDAX TSL OIM™ software showing the crystal rotation at each point with respect to the average orientation of the grain was employed to analyze the collateral damage beneath the craters. After plating the sample surfaces with nickel, it was not possible to directly see the laser spots. The EBSD scans were performed at the expected crater locations with respect to the sample edges after preparing sample cross-sections. The EBSD GROD maps showing craters with the maximum depth and similar width as the diameter of the crater observed from the ablated surface for corresponding laser fluence was considered to be the one obtained just beneath the center of the crater and are reported here.

III. RESULTS AND DISCUSSION

Figure 2 shows the secondary electron (SE) images of the ablation features produced by the single fs laser pulses of various fluence values. Two material removal regions resulting from fs laser ablation of CMSX-4 superalloy are clearly imaged at higher fluence values (Figs. 2(c)–2(f)), i.e., a high damage inner crater region marked as region B (of equivalent diameter $= D2$) and a low damage outer region between $D2$ and $D1$. The rim of the crater is taken as the outer boundary of the high damage region and the low damage region is identified by the contrast difference in the region surrounding the central crater and the un-exposed region on the ablated surface, as seen in Figs. 2(a)–2(f). By examining the variations in the square of the equivalent diameter ($D1$ and $D2$) with the natural logarithm of the laser pulse energy, the beam radius (ω_0), the threshold energy (E_{th}), and the threshold fluence (ϕ_{th}) for different ablation features can be determined using Eq. (1)[18]

$$D^2 = 2\omega_0^2 \ln\left(\frac{\phi}{\phi_{th}}\right) = 2\omega_0^2 \ln\left(\frac{E}{E_{th}}\right). \quad (1)$$

As shown in Fig. 2(g), the ω_0 values are found to be 30 μm and 28 μm based on the variations in the $D1$ and $D2$, respectively. The average of the two ω_0 values ($= 29$ μm) is used for determining the peak fluence values (ϕ) corresponding to different average laser power (p) using $\phi = \frac{2p}{R\pi\omega_0^2}$, where R is the repetition rate ($= 125$ Hz). The threshold fluence values were determined to be 0.49 J/cm^2 and 4.4 J/cm^2, respectively, for the lower and the higher ablation damage features. These values are in good agreement with those reported earlier for CMSX-4.[5,6]

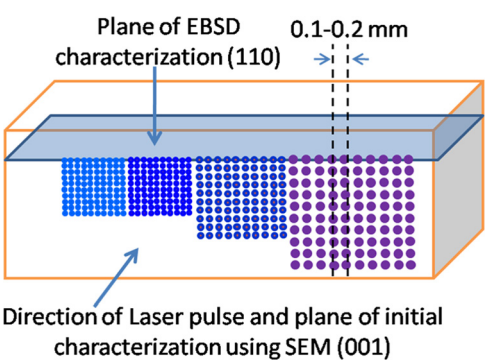

FIG. 1. (Color online) Schematic of the sample for single fs laser pulse ablation and EBSD characterization. Dots indicate individual laser pulses.

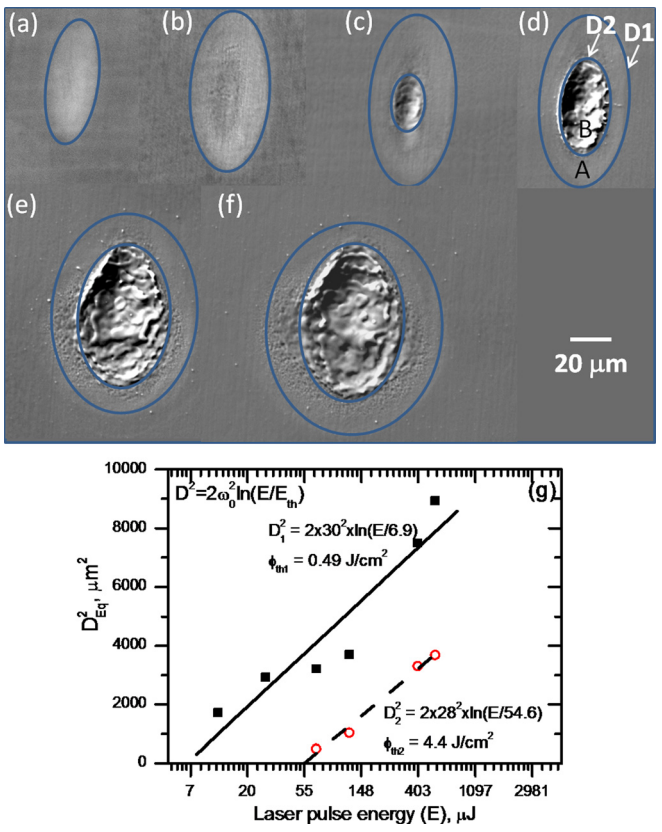

FIG. 2. (Color online) (a)-(f) Typical secondary electron images of the ablation features produced by single fs laser pulse at peak fluence values of (a) 0.9 J/cm^2 (1.5 mw), (b) 2.0 J/cm^2 (3.5 mw), (c) 5.1 J/cm^2 (8.41 mw), (d) 9.1 J/cm^2 (15 mw), (e) 30 J/cm^2 (50 mw), and (f) 41 J/cm^2 (68 mw); (g) variation in square of the equivalent diameter (D_{eq}^2) of the ablated area with single pulse energy.

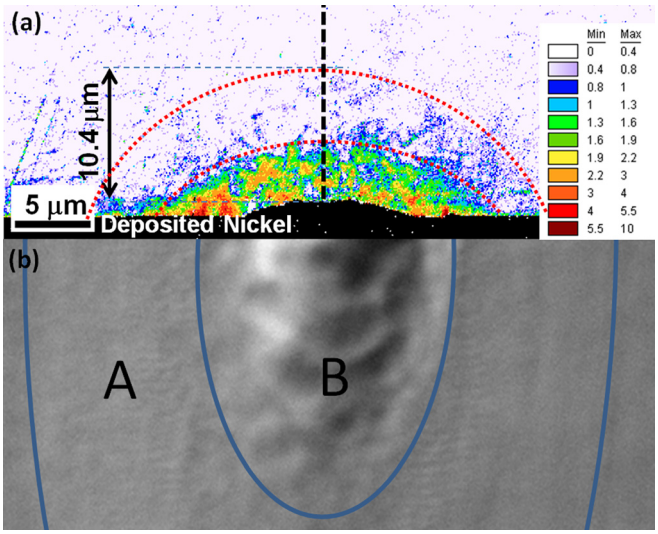

FIG. 3. (Color online) (a) EBSD grain reference orientation deviation (GROD) map (in degrees) obtained beneath the crater produced by a single fs laser pulse of 5.1 J/cm^2 and (b) corresponding secondary electron image (same as Fig. 2(c)) of a crater obtained from the ablated surface. Regions A and B in (b) denote the low and the high damage regions, respectively, on the laser ablated surface. The two red dotted lines in (a) indicate the boundaries of the intense and the low damage regions underneath the crater.

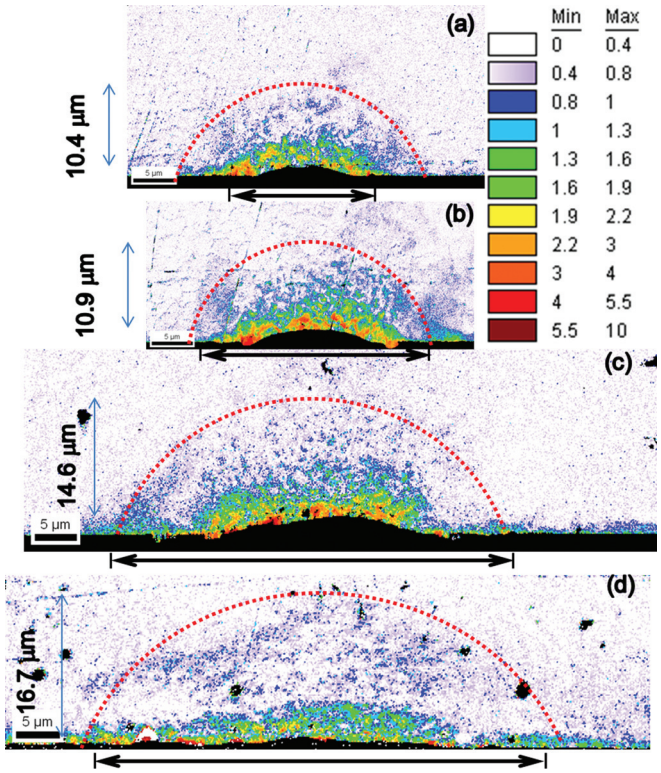

FIG. 4. (Color) GROD maps (in degrees) showing the distribution of damage underneath the craters produced by single fs laser pulse at (a) 5.1 J/cm^2, (b) 9.1 J/cm^2, (a) 30 J/cm^2, and (d) 41 J/cm^2 fluences. The arrows at the bottom of each GROD maps show the extent of the high damage regions on the ablated surface. The width of the low damage regions on the ablated surface were 42 μm, 45 μm, 72 μm, and 87 μm, respectively. The red dotted lines show smooth boundaries of maximum depth of damage as perceived by eyes marking the regions with patches of GROD values higher that ~0.8°. This maximum depth of damage is plotted as a function of fluence in Fig. 5.

Figure 3 shows a typical GROD map obtained from the EBSD analysis on the cross-sectional plane underneath the crater produced by a single fs laser pulse at 5.1 J/cm^2 fluence, in the higher fluence regime. The SE image of a corresponding crater obtained from the ablated surface is also shown at the same magnification for direct comparison. The black area in the GROD map indicates the deposited nickel from which no EBSD pattern could be obtained. A crater of about 1 μm depth in the center of the GROD map is present, followed by a region of about 5 μm depth exhibiting high levels of local crystal rotation, in the range of 1.3°-5°. A second region showing more diffuse damage emanating from the center of the laser-induced crater and extending up to about 10 μm beneath the crater is also apparent in Fig. 3. By comparing the GROD map and the SE image, it is observed that the highest damage intensity is generated in the high fluence ablation region (region B in Figs. 2(d) and 3(b)). No discernible feature typical of laser induced damage, as described above, could be observed underneath the ablation craters produced by single fs laser pulses with fluences of 0.9 and 2.0 J/cm^2, for which the high ablation damage region was not observed on the ablation surface. Similar misorientation distributions as observed underneath the crater produced by single fs laser pulse at a peak fluence of 5.1 J/cm^2 were also observed underneath the craters produced by laser fluences of 9.1, 30, and 41 J/cm^2 with increasing extent of depth and area of damage with increasing fluence, as shown in Figs. 4 and 5. The laser pulses were delivered on the surface that was prepared by conventional metallographic procedures with final polishing using 0.25 μm diamond suspension. This surface was not subjected to vibratory polishing using colloidal silica suspension, as in the case of the surface preparation for EBSD studies. Hence, ~2 μm deep damage layer was observed throughout the surface on which the laser pulses were delivered. This damage layer of about ~2 μm depth is seen at the edges in the EBSD maps in Fig. 4.

The GROD maps provide a good representation of the overall distribution of misorientation developed due to dislocation injection, compared to other measures such as the local misorientation between adjacent sampling points (kernel average misorientation), hence GROD maps are shown

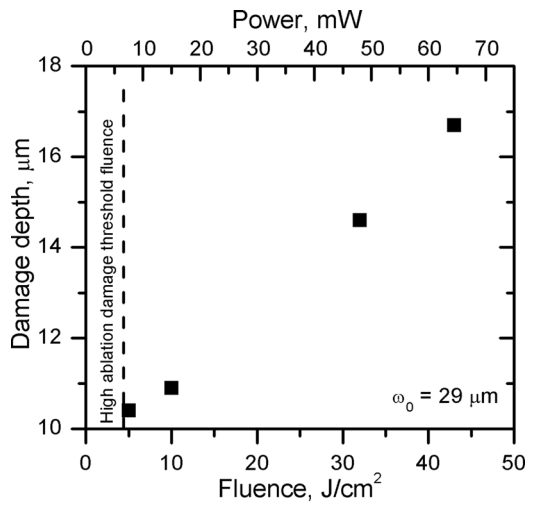

FIG. 5. Variation in the maximum depth of damage with the single fs laser pulse peak fluence.

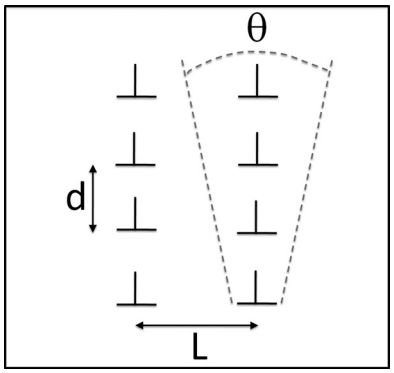

FIG. 6. Relationship between the misorientation, θ, dislocation spacing, d, and scan step size, L.

in this paper. However, to quantitatively analyze the excess dislocation density introduced by the laser pulse, the misorientation between every scan point with respect to the neighboring points is measured at the outer edge of the damage zone (along the dotted line as shown in Fig. 3(a)) and just beneath the ablation crater. Since these misorientations were acquired at slightly different step sizes (0.06-0.18 μm), a correction[19] of 0.26° is given for the misorientation values for all four fluence conditions to match the misorientation per unit length of the undamaged matrix in all the maps. After applying this correction, the misorientation for undamaged matrix is obtained as $\sim 0.4°/\mu$m and the maximum misorientation near the crater is $\sim 4°/\mu$m. Figure 6 schematically shows a simple relationship between the misorientation, θ, dislocation spacing, d, and scan step size, L. Considering that $\theta = b/d$, the dislocation density can be estimated as

$$\rho = \frac{\theta}{bL}. \tag{2}$$

Taking the value of Burgers vector $(1/2\langle 110\rangle)$ as $b = 0.253 \times 10^{-7}$ cm, dislocation densities in the undamaged matrix and near the crater are calculated to be $2.8 \times 10^9/\text{cm}^2$ and $2.8 \times 10^{10}/\text{cm}^2$, respectively. The dislocation density in the undamaged matrix is in good agreement with that reported for the annealed CMSX-4 alloy based on the TEM[20] and synchrotron imaging[21] studies. The 10 times increase in the dislocation density near the crater is also in line with the maximum decrease of 10 times observed in the dislocation spacing with increasing shock pressure from 40 GPa to 55 GPa in [001] Ni single crystal, beyond which it was almost constant up to 65 MPa.[22]

The two different ablation morphologies produced by high fluence single fs laser pulse as observed in the present study have also been reported earlier for various metals and alloys.[5–7,23] The high ablation damage feature has been reported to occur above a threshold beyond which the rate of material removal by ablation abruptly increases.[5,6] Due to the fast energy deposition ensured by the ultrashort laser pulses, the energy is localized into near constant volume of the material, which develops strong pressure waves as material is ejected from the surface, resulting in changes in the structure of the material.[24] It can be seen in Fig. 4 that the collateral damage is confined to the region beneath the surface where fluences are in the high ablation rate regime. This extent of plastic deformation is much less as compared to that reported for nanosecond lasers for similar fluence values where a much larger heat affected zone of about 3–4 times the size of the crater is usually observed.[25] The extent of the laser-induced plastic deformation as revealed by the GROD analysis in the present study is in good agreement with that reported for fs laser ablation study on a superalloy TEM thin film,[9] where a laser-induced plastically deformed layer with a maximum extent of 5 μm including a 2 μm layer of intensively deformed layer was observed by machining with 50-200 pulses at a fluence of 2.33 J/cm^2. A good agreement for the extent of damage observed in the two studies demonstrates that the local crystal rotation based approach followed in the present study for mapping the laser-induced plastically deformed layer indeed provides the distribution of dislocation density underneath the craters.

The damage depth, d, has been measured to be linearly dependent on the fluence, ϕ, Fig. 5. The damaged region contains a high density of dislocations, which will locally increase the hardness of the material beneath the ablated region. For a wide range of metallic materials, it has been shown that the hardness scales with $P^{1/2}$, where P is the peak shock pressure.[26] The defect generation mechanisms that occur in the presence of an attenuating shock wave are complex and remain under investigation.[27] However, since the hardness (and therefore flow stress, σ) of the material is expected to increase with $\rho^{1/2}$,[28] and therefore $\theta^{1/2}$, then the peak pressures associated with the defect generation process would appear to vary linearly with the fluence, ϕ, in the high fluence damage regime, based on Fig. 5. This is in very good agreement with the variation in peak pressure reported to be proportional to $\phi^{0.7\text{-}1.4}$ in various studies.[29,30] In the low fluence regime, no significant increase in misorientation could be measured following ablation. This suggests that dislocations are not easily generated under the conditions present in the low fluence regime. Further hydrodynamic simulations of the shock process would clearly be useful for developing a more detailed model for damage prediction and for correlating defect generation processes with the local stresses present following deposition of the laser pulse.

IV. CONCLUSIONS

1. EBSD based crystal rotation analysis has been used for revealing the laser-induced plastic deformation underneath the craters produced by single fs laser pulses over a range of fluences.
2. The damage is confined to the region beneath the high ablation damage crater and is caused by the shock wave generated in the high damage ablation regime.
3. No discernible damage could be detected beneath the ablation area produced by single fs laser pulse with fluence values below the high ablation damage threshold fluence (<4.4 J/cm^2).
4. Above the high ablation damage threshold fluence, the depth of the laser-induced damage increases linearly with fluence.

ACKNOWLEDGMENTS

The financial support provided by AFOSR in the MURI program (Contract No. FA9550-05-1-0416) for carrying out the present research work is gratefully acknowledged.

[1]X. Liu, D. Du, and G. Mourou, IEEE J. Quantum Electron. **33**, 1706 (1997).
[2]B. N. Chichkov, C. Momma, S. Nolte, F. von Alvensleben, and A. Tunnermann, Appl. Phys. A **63**, 109 (1996).
[3]R. Le Harzic, N. Huot, E. Audouard, C. Jonin, P. Laporte, S. Valette, A. Fraczkiewicz, and R. Fortunier, Appl. Phys. Lett. **80**, 3886 (2002).
[4]A. M. Rubenchik, M. D. Feit, M. D. Perry, and J. T. Larsen, Appl. Surf. Sci. **127**, 193 (1998).
[5]S. Ma, J. P. McDonald, B. Tryon, S. M. Yalisove, and T. M. Pollock, Metall. Mater. Trans. A, **38A**, 2349 (2007).
[6]J. P. McDonald, S. W. Ma, T. M. Pollock, S. M. Yalisove, and J. A. Nees, J. Appl. Phys. **103**, 093111 (2008).
[7]J. Kim and S. Na, Opt. Laser Technol. **39**, 1443 (2007).
[8]N. N. Nedialkov, S. E. Imamova, P. A. Atanasov, G. Heusel, D. Breitling, A. Ruf, H. Hugel, F. Dausinger, and P. Berger, Thin Solid Films **453**, 496 (2004).
[9]Q. Feng, Y. N. Picard, H. Liu, S. M. Yalisove, G. Mourou, T. M. Pollock, in *Superalloys 2004*, edited by K. A. Green, T. M. Pollock, H. Harada, T. E. Howson, R. C. Reed, J. J. Schirra, and S. Walston (The Minerals, Metals & Materials Society (TMS), Warrendale, PA, 2004), pp. 687–696.
[10]A. Borowiec, M. Mackenzie, G. C. Weatherly, and H. K. Haugen, Appl. Phys. A **76**, 201 (2003).
[11]M. A. Meyers, F. Gregori, B. K. Kad, M. S. Schneider, D. H. Kalantar, B. A. Remington, G. Ravichandran, T. Boehly, and J. S. Wark, Acta Mater. **51**, 1211 (2003).
[12]M. Kamaya, A. J. Wilkinson, and J. M. Titchmarsh, Acta Mater. **54**, 539 (2006).
[13]R. Orsund, J. Hjelen, and E. Nes, Scr. Metall. **23**, 1193 (1989).
[14]M. Masimov, Philos. Mag. **87**, 1565 (2007).
[15]N. Zaafarani, D. Raabe, F. Roters, and S. Zaefferer, Acta Mater. **56**, 31 (2008).
[16]J. W. Kysar, Y. X. Gan, T. L. Morse, X. Chen, and M. E. Jones, J. Mech. Phys. Solids **55**, 1554 (2007).
[17]A. J. Wilkinson and P. B. Hirsch, Micron **28**, 279 (1997).
[18]J. Jandeleit, G. Urbasch, H. D. Hoffmann, H. G. Treusch, and E. W. Kreutz, Appl. Phys. A **63**, 117 (1996).
[19]J. Wen and J. Tu, "Deformation mechanisms and strain storage during forging of powder-metallurgy nickel-base turbine disk alloy," Ph.D. thesis (University of Michigan, Ann Arbor, MI, USA, 2010).
[20]T. M. Pollock and A. S. Argon, Acta Metall. Mater. **40**, 1 (1992).
[21]N. S. Husseini, D. P. Kumah, J. Z. Yi, C. J. Torbet, D. A. Arms, E. M. Dufresne, T. M. Pollock, J. Wayne Jones, and R. Clarke, Acta Mater. **56**, 4715 (2008).
[22]H. N. Jarmakani, E. M. Bringa, P. Erhart, B. A. Remington, Y. M. Wang, N. Q. Vo, and M. A. Meyers, Acta Mater. **56**, 5584 (2008).
[23]N. G. Semaltianos, W. Perrie, J. Cheng, P. French, M. Sharp, G. Dearden, and K. G. Watkins, Appl. Phys. A **98**, 345 (2010).
[24]M. A. Meyers, Scri. Metall. **12**, 21 (1978).
[25]A. V. Gorbunov, E. B. Leiko, E. M. Nadgornyi, and S. N. Valkovskii, Scr. Metall. **14**, 417 (1980).
[26]M. C. Meyers, *Dynamic Behavior of Materials* (Wiley, New York, 1994).
[27]N. K. Bourne, G. T. Gray, III, and J. C. F. Millett, J. Appl. Phys. **106**, 091301 (2009).
[28]M. A. Meyers and K. K. Chawla, *Mechanical Behavior of Materials* (Prentice-Hall, Upper Saddle River, NJ, 1999).
[29]C. T. Walters, *in Shock Compression of Condensed Matter - 1991*, edited by S. C. Schmidt, R. D. Dick, J. W. Forbes, and D. G. Tasker (Elsevier Science, Amsterdam), 1992, p. 1.
[30]F. Cottet and M. Boustie, J. Appl. Phys. **66**, 4067 (1989).